Hierarchical Control Design and Performance Assessment of an Ocean Kite in a Turbulent Flow Environment ⋆

James Reed * **Mitchell Cobb** * **Joshua Daniels** *
Ayaz Siddiqui * **Michael Muglia** ** **Chris Vermillion** *

* *Mechanical and Aerospace Eng. Department, North Carolina State University, Raleigh, NC 27603 USA (e-mail: jcreed2@ncsu.edu, mcobb@ncsu.edu, jldanie5@ncsu.edu, asiddiq2@ncsu.edu, cvermil@ncsu.edu)*
** *Renewable Ocean Energy Program, North Carolina Coastal Studies Institute, Wanchese, NC 27981 USA (e-mail: mugliam@ecu.edu).*

Abstract: This paper presents a hierarchical control framework for a kite-based marine hydrokinetic (MHK) system that executes power-augmenting cross-current flight, along with simulation results based on a high-fidelity turbulent flow model that is representative of flow conditions in the Gulf Stream. The hierarchical controller is used to robustly regulate both the kite's flight path and the intra-cycle spooling behavior, which is ultimately used to realize net positive energy production at a base station motor/generator system. Two configurations are examined in this paper: one in which the kite is suspended from a surface-mounted platform, and another in which the kite is deployed from the seabed. To evaluate the robustness of this control framework in a realistic ocean environment, we present simulation results whereby we superimpose low-frequency data from the Mid Atlantic Bight South Atlantic Bight Regional Ocean Modeling System and acoustic Doppler current profiler measurements with a high-frequency turbulence model, resulting in a high-fidelity 3D spatiotemporal flow field that is presented to the kite system. Based on this simulation framework, we demonstrate the effectiveness of the control system both in terms of robust flight and power generation.

Keywords: Energy systems, Marine systems, Emerging control systems, Hierarchical control, Periodic control

1. INTRODUCTION

Marine hydrokinetic (MHK) resources have been estimated to possess as much as 1229 TW/year of wave energy (Jacobson (2011)), 334 TWh/year of usable tidal energy (Haas et al. (2011)), and 163 TWh/year of usable ocean current energy (Haas et al. (2013)) within the United States alone. This collective MHK resource is sufficient to power tens of millions of homes, in addition to powering oceanographic research buoys, navigational buoys, autonomous underwater vehicles, and other entities that comprise the so-called "blue economy" (LiVecchi et al. (2019)). However, economically practical extraction of MHK resources is complicated by the large required size of such devices (for example, a fixed ocean turbine operating in a 1 m/s flow speed must be approximately as large per unit power as a towered wind energy system operating in a 10 m/s wind speed, yet the costs of building such a device underwater are much larger) and the locations in which these resources exist (for example, the strongest portion of the Gulf Stream routinely lies in waters that are at least 1 km deep, as noted in Zeng and He (2016)).

Underwater kites represent a relatively new technology for harvesting tidal and current resources using an order of magnitude less material than fixed turbines. Depicted in Fig. 1, a kite-based MHK system consists of a rigid wing that is tethered to either the seabed or a surface platform and flown in a pattern *perpendicular* to the prevailing current. Energy can be generated either through on-board rotors (Minesto (2019)) or through cyclic spooling motion (Ghasemi et al. (2015)), whereby tether is spooled out under high tension and spooled in under low tension, resulting in net positive energy generation at a winch located on the seabed/platform. As shown in Loyd (1980), for a high lift/drag wing, this *cross-current* motion can easily result in more than an order of magnitude more power than that of a stationary system of the same size. The ability to achieve such high power density has led to the popularization of kite-based systems not only for harvesting MHK resources, but also in the sister field of airborne wind energy, as practiced by companies like Windlift, LLC (Windlift (2019)), Makani Power (Makani (2019)), and Ampyx Power (Ampyx (2019)).

This work will focus specifically on an MHK kite design that generates net energy through cyclic spooling motion, which can in general be accomplished in one of two ways, or a combination thereof:

⋆ This research is supported by the Department of Energy, award number DE-EE0008635.

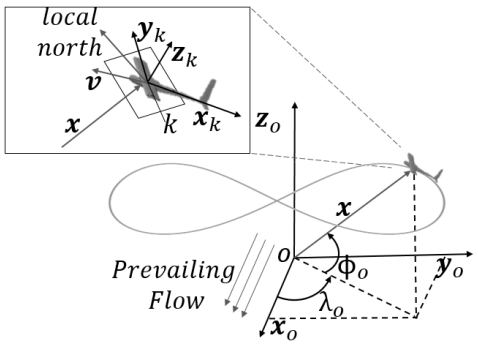

Fig. 1. Concept of operations for cross-current figure-8 flight, including body-frame and ground-frame coordinate systems represented by three orthonormal unit vectors, $\boldsymbol{x}_k$, $\boldsymbol{y}_k$, and $\boldsymbol{z}_k$ with origin k and orthonormal unit vectors $\boldsymbol{x}_o$, $\boldsymbol{y}_o$, and $\boldsymbol{z}_o$ with origin o respectively. Additionally, spherical coordinate angles λ_o and ϕ_o and the vector from o to k, (denoted as $\boldsymbol{x}$) are shown.

(1) *multi-cycle spooling*, where tether is continually spooled out under high tension over multiple laps (where a lap is one complete traversal of a path), and spooled in under low tension either radially towards the base station or in a path following configuration under low-tension, low-lift flight, or
(2) *intra-cycle spooling*, where the spooling rate is adjusted over the course of each lap, spooling tether out at high angles of attack on portions of the path corresponding to high tension, and spooling tether in at low angles of attack on portions of the path corresponding to low tension.

Several studies, including Ghasemi et al. (2015), Ghasemi et al. (2016), Olinger and Wang (2015), and Li et al. (2015), have presented hydrodynamic characterizations, dynamic models, and corresponding controllers for MHK kites. These models have been validated in simulations, as well as controlled pool and flume tests. While these works provide meaningful modeling contributions, the results are restricted to spatiotemporally uniform flow environments. Thus, additional questions remain regarding how well the MHK kite control systems will perform, in terms of robustness and power production, in realistic ocean environments that consist of both low-frequency (LF) spatiotemporal flow variations and high-frequency (HF) turbulence. While performance in turbulent conditions has been studied in the sister field of kite-based *wind* energy systems (for example, in Sternberg et al. (2012) and Fechner and Schmehl (2016)), in addition to the field of *stationary* MHK systems in Mycek et al. (2014) and Pyakurel et al. (2017), the dissimilar time and length scales of ocean currents, in addition to the different system dynamics of kites vs. stationary systems, motivate kite-specific studies in realistic ocean environments.

This work contributes to the existing body of literature by presenting a hierarchical flight control system and intra-cycle spooling controller for an MHK kite, which is shown to be robust in the presence of a realistic turbulence environment. To demonstrate this robust performance, we present simulation results in a turbulent environment that consists of the superposition of two components:

(1) A LF profile, taken from either observed acoustic Doppler current profiler (ADCP) readings or a Mid Atlantic Bight/South Atlantic Bight Regional Ocean Model System (MSR) detailed in Yang and Copping (2017) (one or the other is used in all of our simulations, depending on availability of ADCP data). This provides the evolution of flow speed with respect to both depth and time, over relatively long time intervals.
(2) A HF turbulence model, adopted from Pyakurel et al. (2017), which characterizes flow variations in depth, cross-current location, and time, over time scales of seconds.

2. PLANT MODEL

Following our earlier work in Reed et al. (2019), the MHK kite is modeled as a combination of a rigid lifting body wherein forces and moments are calculated from lift, drag, buoyancy, and gravity, and a lumped mass tether model whose links are characterized as non-compressive spring-damper systems, as in Vermillion et al. (2014). The instantaneous mechanical power produced by the system $P_{gen}(t)$, is modeled as:

$$P_{gen}(t) = ||\boldsymbol{F}_{thr}||\tilde{u}_T(t), \tag{1}$$

where $\tilde{u}_T(t)$ is the spool speed of the tether, and $\boldsymbol{F}_{thr}$ is the force from the tether.

3. REALISTIC OCEAN CURRENT MODELING AND IMPLEMENTATION

The flow field, which is characterized as a function of depth ($\boldsymbol{z}_o$), cross-current location ($\boldsymbol{y}_o$), and time (t), is computed as the superposition of a LF flow profile and HF turbulence model, as:

$$\tilde{V}_{comb}(\boldsymbol{y_o}, \boldsymbol{z_o}, t) = \tilde{V}_{turb}(\boldsymbol{y_o}, \boldsymbol{z_o}, t) + \tilde{V}(\boldsymbol{z_o}, t), \tag{2}$$

where $\tilde{V}(\boldsymbol{y_o}, \boldsymbol{z_o}, t)$, $\tilde{V}_{turb}(\boldsymbol{y_o}, \boldsymbol{z_o}, t)$, and $\tilde{V}_{comb}(\boldsymbol{y_o}, \boldsymbol{z_o}, t)$ represent the LF flow field, HF turbulent field, and combined flow model, respectively. Because the total cross-current motion of the kite spans a tiny fraction of the total current resource (e.g., the Gulf Stream), spatial variations in $\boldsymbol{y}_o$ are neglected in the LF model.

3.1 Low-Frequency Ocean Modeling

When available, observed ADCP data, collected by the Renewable Ocean Energy Program of the Coastal Studies Institute, was used to characterize LF flow variations. This data profiles a location about 20 miles east of Cape Hatteras, NC on the shelf slope and is available at 10-minute time intervals and 4 m vertical resolution. Because the ADCP data is specific to a particular location and is not usable in the top 40 m of the water column due to surface reflections, MSR data was used as an alternative when simulating kite deployment of a sea surface platform (e.g., a fixed buoy). The MSR model was generated by North Carolina State University's Ocean Observing and Modeling Group, and provides current profiles at 42 different locations in the Gulf Stream at 25 m vertical resolution. Each data set provides flow velocity vectors, $\tilde{V}(\boldsymbol{z_o}, t)$, along the water column (i.e., the $\boldsymbol{z_o}$ direction).

3.2 Modeled High-Frequency Turbulent Variability

The turbulent HF components of the ocean currents are calculated based on a discretization of the flow velocity's power spectral density (PSD) equation. Specifically, the model leverages fundamental techniques described in Pyakurel et al. (2017) to generate a spatiotemporally varying turbulence profile that can be applied to the hydrodynamic center of each component in the dynamic model. Based on inputs of turbulence intensity, time-averaged flow velocity profile, a specified frequency range, standard deviations and spatial correlation coefficients for the flow velocities, the model outputs a spatial grid of time-varying velocity vectors on the inlet plane (which is n_y by n_z, having indices i and j ranging from 1 to n_y and 1 to n_z). The continuous PSD of flow velocity, $G(f)$, where f represents frequency, is given as:

$$G(f) \propto f^{-\frac{5}{3}}, \tag{3}$$

which implies G^m, the one-sided PSD, is equal to:

$$G^m(f) = A_m f^{-\frac{5}{3}}. \tag{4}$$

Here, A_m is a constant defined by the equation:

$$A_m = \frac{2\overline{U}^2 T_m^2}{3\left[\frac{1}{f_{min}^{\frac{2}{3}}} - \frac{1}{f_{max}^{\frac{2}{3}}}\right]}, \tag{5}$$

where m is an index to the u, v, or w velocity components, f_{min} and f_{max} define the frequency range of the turbulence, $\overline{U}$ is the magnitude of the time-averaged flow velocities, $\overline{u}$, $\overline{v}$, and $\overline{w}$, defined as:

$$\overline{U} = \sqrt{\overline{u}^2 + \overline{v}^2 + \overline{w}^2}, \tag{6}$$

and where turbulence intensity, denoted by T_m, is equal to:

$$T_m = \frac{\sigma_m}{\overline{U}}, \tag{7}$$

where the standard deviations (σ_m) in the axial, cross-current, and down directions are calculated as:

$$\sigma_u = \frac{T_u}{\sqrt{1+P^2+Q^2}}, \sigma_v = P\sigma_u, \text{ and } \sigma_w = Q\sigma_u. \tag{8}$$

Here, P and Q are constants defining the ratios between the standard deviations of the flow velocities in the cross-current and down directions over the standard deviation in the axial direction.

Correlated velocity components are then generated by a discretized one-sided PSD equation, $\tilde{s}^m(\boldsymbol{f})) = G^m(f)\delta f$, where $\boldsymbol{f}$ is the vector of user-selected frequencies, chosen to capture the characteristic frequencies of the flow field, $\boldsymbol{f} \triangleq f_1, f_2 ..... f_n$. A coherence function, C_{ij}, defining the flow component's correlation between any two grid nodes on the inlet plane, is defined by:

$$C_{ij}(\boldsymbol{f}) = \exp\left(-\frac{R_c \Delta r_{ij} \boldsymbol{f}}{\overline{U}}\right), \tag{9}$$

where Δr_{ij} is the distance between any two inlet plane grid nodes and R_c is a coherence decay constant. The amplitude of the fluctuating velocity component, S^m, is written as:

$$S_{ij}^m(\boldsymbol{f}) = 2C_{ij}(\boldsymbol{f}) A_m(f)^{-\frac{5}{3}} \delta f. \tag{10}$$

The velocity weighting factor, $H(\boldsymbol{f})$, is then calculated in frequency domain as:

$$\begin{aligned}
H_{11}^m(\boldsymbol{f}) &= S_{11}^m(\boldsymbol{f})^{\frac{1}{2}}, H_{21}^m(\boldsymbol{f}) = \frac{S_{21}^m(\boldsymbol{f})}{H_{11}^m(\boldsymbol{f})}, \\
H_{22}^m(\boldsymbol{f}) &= (S_{22}^m(\boldsymbol{f}) - H_{21}^m(\boldsymbol{f})^2)^{\frac{1}{2}}, H_{31}^m(\boldsymbol{f}) = \frac{S_{31}^m(\boldsymbol{f})}{H_{11}^m(\boldsymbol{f})}, \\
H_{ij}^m(\boldsymbol{f}) &= \frac{(S_{ij}^m(\boldsymbol{f}) - \sum_{l=1}^{l=j-1} H_{il}^m(\boldsymbol{f}) H_{jl}^m(\boldsymbol{f}))}{H_{jj}^m(\boldsymbol{f})}, \\
H_{jj}^m(\boldsymbol{f}) &= (S_{jj}^m(\boldsymbol{f}) - \sum_{l=1}^{l=j-1} H_{jl}^m(\boldsymbol{f})^2)^{\frac{1}{2}},
\end{aligned} \tag{11}$$

where H_{ij}^m is the element in the i^{th} row and the j^{th} column of $H \in \mathbb{R}^{n_y n_z \times n_y n_z}$. The velocity weighting factor, $H_{ij}^m(\boldsymbol{f})$, is then used to calculate analytical expressions for the velocity components, u, v, and w, as functions of time. The amplitude of the fluctuating velocity component, m_{kj}^*, can be represented as

$$m_{kj}^* = \sum_{l=1}^{j} H_{lj}^m(f_k) e^{i\theta_{kl}}, \tag{12}$$

where θ_{kl} is a random phase angle between 0 and 2π. Because $m_{kj}^* = |m_{kj}^*| e^{i\theta_{kj}}$, where θ_{kj} is the resultant phase angle associated with each frequency component at each grid point, j, m_{kj}^* can be converted from frequency domain to time domain, where each fluctuating velocity component is denoted as:

$$m_j(t) = \sum_{k=1}^{N} |m_{kj}^*| \sin(2\pi f_k^* t + \theta_{kj}). \tag{13}$$

This calculation results in a grid of velocity vectors, $\tilde{V}_{turb}(\boldsymbol{y_o}, \boldsymbol{z_o}, t)$, at each node of the inlet plane.

4. CONTROL FORMULATION

The control system is designed to achieve two objectives: (i) Traverse a prescribed cross-current path that results in high tether tensions and (ii) strategically switch between spool-out and spool-in behavior in a manner that keeps the kite in a relatively consistent depth and flow range. The former is accomplished via a hierarchical controller, whereas the latter is accomplished through an intra-cycle spooling controller. The complete control system block diagram is shown in Fig. 2.

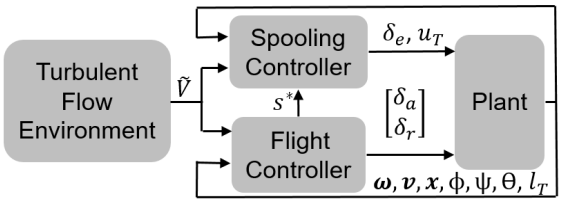

Fig. 2. Block diagram of kite system where $\boldsymbol{\omega}$ is the angular velocity vector and $\boldsymbol{v}$ is the velocity vector of the kite in the body-frame. Additionally, ϕ, θ, and ψ are the roll, pitch, and yaw Euler angles respectively, and l_T is the un-spooled tether length.

4.1 Flight Controller

As described in our earlier work in Reed et al. (2019), the flight controller which enables the kite to track a prescribed figure-8 path, contains four levels. This modular,

hierarchical control structure is based on prior work in Rapp et al. (2019) and is partitioned into:

(1) A *path following controller* that accepts the path geometry and outputs a desired velocity angle as defined in Fagiano et al. (2014).
(2) A *tangent roll angle controller*, which accepts a desired velocity angle, $\gamma(\boldsymbol{v}_{des})$, and outputs a desired tangent roll angle, ξ_{des}, which is the angle between $\boldsymbol{y}_k$ and the plane tangent to the surface of the sphere of radius $\|\boldsymbol{x}\|$ at the kite's position, termed the *tangent plane* (shown in Fig. 1) – this angle dictates the component of hydrodynamic lift that contributes to turning.
(3) A *desired moment controller*, which accepts the tangent roll setpoint and side-slip angle setpoint, and outputs a desired moment vector.
(4) A *control allocation module*, which accepts the desired moment vector and computes the required control surface deflections to be actuated by the ailerons, elevators, and rudder of the kite.

Path Following Controller The target cross-current path, $\boldsymbol{\Gamma}(s)$, is specified in Cartesian coordinates based on the Lemniscate of Booth, defined by a_{booth} and b_{booth} shown in Rapp et al. (2019). The variable s is a path parameter that varies from 0 to 2π. Given this path, the controller calculates a three-dimensional vector representing the desired direction of the kite's velocity vector, which is computed as a weighted average between the *perpendicular vector*, $\boldsymbol{p}_{\perp}^{*}$, and the *parallel vector*, $\boldsymbol{p}_{\parallel}^{*}$. The perpendicular vector is given by:

$$\boldsymbol{p}_{\perp}^{*} = \frac{\hat{p}_{\perp}}{\|\hat{p}_{\perp}\|} \quad \text{where} \quad \hat{p}_{\perp} = \begin{bmatrix} (\boldsymbol{\Gamma}(s^*) - \boldsymbol{x}) \cdot \boldsymbol{u}_{\phi_o}(\boldsymbol{x}) \\ (\boldsymbol{\Gamma}(s^*) - \boldsymbol{x}) \cdot \boldsymbol{u}_{\lambda_o}(\boldsymbol{x}) \\ 0 \end{bmatrix}. \quad (14)$$

Here, $\boldsymbol{u}_{\phi_0}(\boldsymbol{x})$ and $\boldsymbol{u}_{\lambda_o}(\boldsymbol{x})$ are unit vectors in the elevation (ϕ) and azimuth (λ) directions shown in Fig. 1, sometimes referred to as "local north" and "local east." The parallel vector, $\boldsymbol{p}_{\parallel}^{*}$, is a unit vector that lies parallel to the path at the path variable corresponding to the closest point on the path, s^*, and is calculated by:

$$\boldsymbol{p}_{\parallel}^{*} = \frac{\hat{p}_{\parallel}}{\|\hat{p}_{\parallel}\|} \quad \text{where} \quad \hat{p}_{\parallel} = \left.\frac{d\boldsymbol{\Gamma}}{ds}\right|_{s=s^*}. \quad (15)$$

In (14) and (15), the closest point on the path is described by the path variable s^*, which is the solution to the minimization problem:

$$s^* = \arg\min_{s} \ \alpha(s), \quad \text{where}$$
$$\tan(\alpha(s)) = \frac{\|\boldsymbol{x} \times \boldsymbol{\Gamma}(s)\|}{\boldsymbol{x} \cdot \boldsymbol{\Gamma}(s)}. \quad (16)$$

Here, $\alpha(s)$ is the angle between the position vector, $\boldsymbol{x}$ and the path $\boldsymbol{\Gamma}(s)$.

The desired velocity unit vector, $\boldsymbol{v}_{des}$, is then calculated as the linearly weighted sum of $\boldsymbol{p}_{\perp}^{*}$ and $\boldsymbol{p}_{\parallel}^{*}$, according to:

$$\overline{\alpha}(s^*) = \min\left\{\alpha(s^*), \alpha_0\right\}$$
$$\boldsymbol{v}_{des} = \left(1 - \frac{\overline{\alpha}(s^*)}{\alpha_0}\right)\boldsymbol{p}_{\parallel}^{*} + \frac{\overline{\alpha}(s^*)}{\alpha_0}\boldsymbol{p}_{\perp}^{*}. \quad (17)$$

Here, α_0 serves as an upper limit on the angle used in the weighting.

The velocity angle, γ, which describes the orientation of a given velocity vector on the sphere of radius $\|\boldsymbol{x}\|$ at the current position $\boldsymbol{x}$, is given by

$$\gamma(\boldsymbol{v}) = \operatorname{atan}\left(\frac{\boldsymbol{v} \cdot \boldsymbol{u}_{\phi_o}(\boldsymbol{x})}{\boldsymbol{v} \cdot \boldsymbol{u}_{\lambda_o}(\boldsymbol{x})}\right). \quad (18)$$

The desired velocity angle is therefore given by $\gamma(\boldsymbol{v}_{des})$.

Tangent Roll Angle Controller The next level of the flight controller maps $\gamma(\boldsymbol{v}_{des})$ to a desired tangent roll angle, ξ_{des}, where ξ describes the kite's orientation relative to the tangent plane and is calculated as:

$$\tan(\xi(\boldsymbol{y}_k(t))) = \frac{\boldsymbol{y}_k \cdot (\boldsymbol{u}_{\lambda_o} \times \boldsymbol{u}_{\phi_o})}{\sqrt{(\boldsymbol{y}_k \cdot \boldsymbol{u}_{\phi_o})^2 + (\boldsymbol{y}_k \cdot \boldsymbol{u}_{\lambda_o})^2}}. \quad (19)$$

The desired tangent roll angle, ξ_{des}, is calculated using saturated proportional control, specifically:

$$\xi_{des} = \min\{\max\{k_\gamma\left(\gamma(\boldsymbol{v}) - \gamma(\boldsymbol{v}_{des})\right), \xi_{min}\}, \xi_{max}\}, \quad (20)$$

where k_γ is the proportional gain. Ultimately, adjustment of ξ re-vectors the kite's lift to provide the necessary force to re-align the kite's velocity angle with the target value and ultimately get the kite back on its target path.

Desired Moment Vector Controller In selecting the desired moments, we set a target rolling moment to drive the tangent roll angle (ξ) to its setpoint (ξ_{des}), whereas we set a target yaw moment to drive the side-slip angle, β, to zero. The tether spooling controller articulates the elevator to trim the system to a high angle of attack during spool out and a low angle of attack during spool in (which is described in the subsequent sub-section). The desired moment vector set within the flight controller is given by:

$$\boldsymbol{M}_{des} = \begin{bmatrix} k_{p_L} e_\xi(t) + k_{i_L} \int_0^t e_\xi(t)d\tau + k_{d_L}\dot{e}_\xi(t) \\ 0 \\ k_{p_N}\beta + k_{i_N}\int_0^t \beta d\tau + k_{d_N}\dot{\beta} \end{bmatrix},$$

where $e_\xi(t) = \xi(\boldsymbol{y}_k(t)) - \xi_{des}$, and β is the fluid dynamic side-slip angle.

Control Allocation Module In order to map the desired moment vector to control surface deflections, we invert a linearized approximation of the nonlinear mapping from deflections to hydrodynamic moments. This approximation is calculated by neglecting the effect of angular velocity on the apparent flow at each fluid dynamic surface, then linearizing to obtain an expression in the following form:

$$\boldsymbol{M}_{net} = \boldsymbol{M}_o + A\boldsymbol{\delta}, \quad (21)$$

where $\boldsymbol{\delta} \triangleq [\ \delta_a\ \delta_e\ \delta_r\ ]^T$ represents the deflection angles of the ailerons, elevator, and rudder, respectively. The variable $\boldsymbol{M}_o$ represents the moment vector that occurs with zero control surface deflections and A is the matrix of linear control sensitivity coefficients. This results in a system of three equations and three unknowns, which are solved in computing the control surface deflections at each time.

4.2 Winch (Spooling) Controller

The commanded rate of tether release, $u_T(t)$, is set by a spooling controller that seeks to spool tether out at a high angle of attack during the portions of the lap in which large tensions are possible, then spool tether in at a low angle

of attack during the remainder of the lap. The intra-cycle spooling algorithm in this work is designed to maintain a consistent tether length each lap, represented by the constraint:

$$\int_{t_{0,j}}^{t_{f,j}} \tilde{u}_j(\tau)d\tau = 0. \tag{22}$$

where the index j refers to the lap number. This ensures that the kite remains in a consistent depth within the ocean shear profile. In attempting to find the command sequence that satisfies this constraint, we make several key simplifying assumptions:

- The winch is capable of achieving the commanded speed.
- The winch is capable of achieving that speed quickly, relative to the rate of change of the command.
- The commanded spooling speed is piecewise constant over each of N_R "spooling regions", and alternates between spooling in and spooling out at the maximum speed, u_{spool}.

The first two approximations should hold for a well designed winch/generator system, meaning that $\tilde{u}_T(t) \approx u_T(t)$. The three approximations together mean that the constraint equation of (22) can be written as:

$$0 = \mathbf{1}^{1\times N_R}\underline{U}^{j-1}\Delta_T^j, \tag{23}$$

where the matrix $\underline{U}^{j-1} \in \mathbb{R}^{N_R\times N_R}$ is a diagonal matrix where the element in the p^{th} and q^{th} column is given by:

$$\underline{U}_{p,q}^{j-1} = \begin{cases} u_{spool}^{j-1} & p = q = \text{odd} \\ -u_{spool}^{j-1} & p = q = \text{even} \\ 0 & p \neq q. \end{cases} \tag{24}$$

Here, u_{spool}^{j-1} is one third of the mean flow speed at the vehicle CM over the last lap of the system. The vector $\Delta_T^j \in \mathbb{R}^{N_R}$ is a vector containing the time durations required to traverse a specific section of the path during next (j^{th}) lap. Because the timings of the next lap are not known beforehand, it is desirable to define our tether spooling controller in terms of the path variable, s, *not* time. Therefore, we transform the time-domain constraint of (23) to a path-domain constraint by using a numerical approximation of the time derivative of the path variable from the previous lap in each spooling region. Here, we denote the spooling region with the index $i_R = 1, 2, \ldots, N_R$. Specifically, we approximate the i_R^{th} element of Δ_T^j, written as Δ_{T,i_R}^j in terms of the path variable using logged data from the previous lap, $j-1$. Specifically,

$$\Delta_{T,i_R}^j \approx \frac{s_{i_R+1}^{j-1} - s_{i_R}^{j-1}}{\delta s_{i_R}^{j-1}} \tag{25}$$

$$= \begin{bmatrix} \frac{1}{\delta s_1^{j-1}} & 0 & \ldots & 0 \\ 0 & \frac{1}{\delta s_2^{j-1}} & \ldots & 0 \\ \vdots & \vdots & \ddots & \vdots \\ 0 & 0 & 0 & \frac{1}{\delta s_{N_R+1}^{j-1}} \end{bmatrix} \underline{D} \begin{bmatrix} s_1^{j-1} \\ s_2^{j-1} \\ \vdots \\ s_{N_R+1}^{j-1} \end{bmatrix} \tag{26}$$

$$\triangleq \underline{\delta s}^j \underline{D} S^{j-1}. \tag{27}$$

Note that $s_{i_R}^{j-1}$ refers to the value of the path variable at the end of the i_R^{th} region during the previous lap, $j-1$. Additionally, $\delta s_{i_r}^{j-1}$ is the mean of the derivative of $s(t)$ over the i_R^{th} section of the path. Furthermore, because the path is defined using a path variable $s \in \{0, 1\}$, $s_{N_R+1}^j = 1$ for all j. The discrete difference operation matrix $\underline{D} \in \mathbb{R}^{N_R\times N_R}$ is a matrix with ones along the main diagonal and negative ones on the diagonal underneath the main diagonal. Thus, after every lap, the problem of meeting our approximation of the net-zero spooling constraint becomes one of solving an approximated version of the constraint equation,

$$0 = \mathbf{1}^{1\times N_R}\underline{U}^{j-1}\underline{\delta s}^{j-1}\underline{D}S^j, \tag{28}$$

for the vector $S^j \in R^{N_R+1}$, the elements of which define the spooling regions for the next lap. Note that in general, this is a single scalar equation and cannot be solved uniquely for the elements of S^j. However, if we prescribe a structure to the spooling regions, we can reduce the number of parameters that define the spooling regions to one, resulting in a unique solution. In the case of the figure-8 path geometry, we know that the tension profile over the course of a figure-8 exhibits two local minima, which occur roughly at $s = 0.25$ and $s = 0.75$. Therefore, our vector S^j takes the form

$$S^j = \begin{bmatrix} 0.25 \\ 0.25 \\ 0.75 \\ 0.75 \\ 1 \end{bmatrix} + \begin{bmatrix} -1 \\ 1 \\ -1 \\ 1 \\ 0 \end{bmatrix} s_w^j. \tag{29}$$

By substituting this expression into (28), we can solve directly for s_w^j, which defines the width of the spooling region for the next lap. This then defines a simple, switched spooling control structure:

$$\mathbf{u}_T^j(s^*(t)) = \begin{cases} u_{in} & 0.25 - s_w^j \leq s^*(t) \leq 0.25 + s_w^j \text{ or} \\ & 0.75 - s_w^j \leq s^*(t) \leq 0.75 + s_w^j, \\ u_{out} & \text{otherwise.} \end{cases} \tag{30}$$

While (30) will yield zero net spooling under *nominal* conditions, it is not robust to disturbances that cause the actual flight speed (and therefore the time required to traverse a particular section of the figure-8) to differ from that which was used in computing $\mathbf{u}_T^j(s^*(t))$. To add robustness to the spooling strategy, we utilize a simple feedback controller to track a target tether length, $l_{T,SP}^j(s(t))$, which is obtained by integrating (30) over the path as follows:

$$l_{T,SP}^j(s(t)) = l_{T,0} + \int_0^{s(t)} \frac{\mathbf{u}_T^j(\sigma)}{\delta s^{j-1}} d\sigma. \tag{31}$$

5. RESULTS

This section details two sets of simulation results, one in which the kite is deployed from a floating platform at the sea surface, and another in which the kite is deployed from the seabed. Because the ADCP data is invalid at low depths due to surface reflections, the MSR model is used to characterize the LF component of flow in the former case (to be referred to as the MSR case in simulation results), whereas ADCP data is used to characterize the LF component of flow in the latter case (to be referred to as the ADCP case in simulation results). In both simulation cases, an average tether length of 125 m is used. For comparison purposes, two additional simulations were

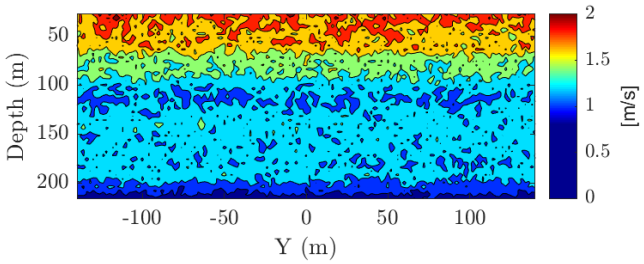

Fig. 3. One instant in time of the $\boldsymbol{x_o}$ component of flow velocity in the $\boldsymbol{y_o}$, $\boldsymbol{z_o}$ plane for the ADCP data with superimposed turbulence

performed under spatiotemporally constant flow profiles, both at an average tether length setpoint of 125m, where the constant flow speeds were set to the average flow speeds seen in the MSR and ADCP data. By comparing our results against constant flow simulations, we were able to assess the effects of turbulence on the kite's power production. An example plot of the total $\boldsymbol{x_o}$ component of flow velocity at the inlet plane (including both the LF flow and HF turbulence), for a single time step, is shown in Fig. 3, using ADCP data for the LF component. The parameters used in the simulations are shown in Table 1. Additionally, the average power produced in the MSR and ADCP simulation sets, along with the constant flow results, are shown in Table 2, as a function of average tether length setpoint and mean flow speed at the kite's center of mass.

Table 1. Parameters used in simulation.

Variable	Description	Value	Units
A_r	Kite reference area	10	m^2
m_k	Kite mass	945	kg
–	Kite span	10	m
a_{booth}	Height path parameter	0.8	-
b_{booth}	Width path parameter	1.6	-
f_{max}	Maximum turbulent frequency	1	s^{-1}
f_{min}	Minimum turbulent frequency	0.1	s^{-1}
T	Turbulence intensity	10	%

5.1 Simulation Results

A plot of the flow speed at the kite's center of mass over two laps is shown in Fig. 4, for both the MSR and the ADCP example simulations. The periodic behavior that we observe in Fig. 4 results from the higher flow speeds experienced near the top of the path, which is a direct result of the ocean's velocity profile, an example of which can be seen in Fig. 3. The velocity of the kite over two laps can be seen in Fig. 5 for both the MSR and ADCP example simulations. Additionally, the tether tension magnitude, $||\boldsymbol{F}_{thr}||$, is shown in Fig. 6 for both the ADCP and MSR example simulations. The average power per lap is shown in Fig. 7 and Fig. 8 for the ADCP and MSR example simulations, along with the constant flow simulations (which were run at the same average flow speeds as the MSR and ADCP example simulations to provide a comparison of the kite's power production in constant flow vs. turbulent environments). The average power produced in the MSR example simulation was 23.9 kW at an average flow speed of 1.43 $\frac{m}{s}$, which is

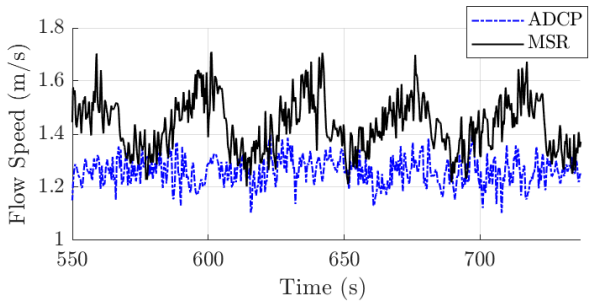

Fig. 4. Flow speed at the kite's CM over two laps for the MSR and ADCP example simulations

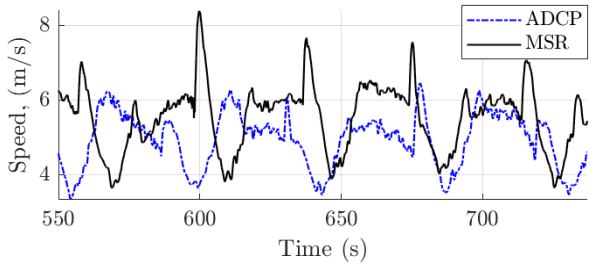

Fig. 5. The kite's speed over two laps for the MSR and ADCP example simulations

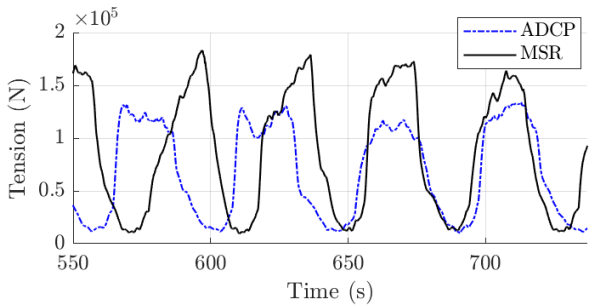

Fig. 6. The magnitude of tether tension over two laps for the MSR and ADCP example simulations

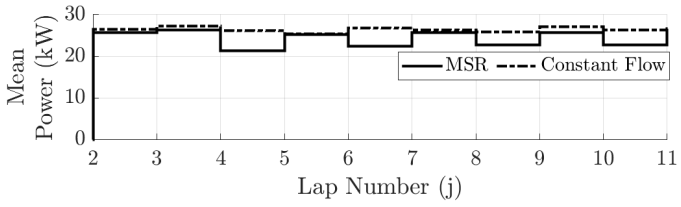

Fig. 7. This plot shows the average power produced over each lap for the constant flow and MSR simulations, both with the same average flow speed.

90.5% of the average power produced in its constant flow simulation, which was 26.4 kW. In the ADCP example simulation, the average power produced was 16.4 kW at an average flow speed of 1.26 $\frac{m}{s}$, which was 87.2% of the power produced in the constant flow simulation, which was 18.8 kW. Additionally, it is clear from the simulations that the kite robustly executes cross-current flight in the presence of turbulence.

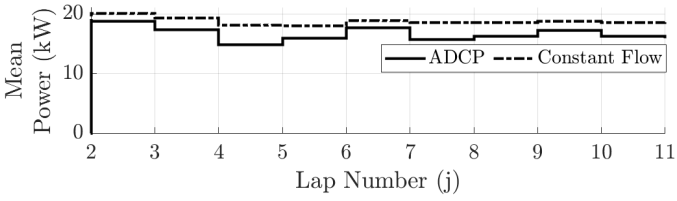

Fig. 8. This plot shows the average power produced over each lap for the constant flow and ADCP simulations, both with the same average flow speed.

Table 2. Parameters used in simulation.

Simulation set	Average Tether length setpoint (m)	Mean flow speed (ms^{-1})	Mean power output (kW)
MSR	50	1.56	29.6
MSR	125	1.43	23.9
Const. flow - MSR avg.	125	1.43	26.4
MSR	200	1.27	15.1
ADCP	50	1.17	14.4
ADCP	125	1.26	16.4
Const. flow - ADCP avg.	125	1.26	18.8
ADCP	200	1.27	17.1

6. CONCLUSION

In this paper, the first implementation of a tethered MHK kite with closed-loop control of cross-current flight in a turbulent ocean flow environment was presented. This was performed by generating two spatiotemporally varying ocean current profiles, using data from the MRS model for the first and observed ADCP data for the second, both with superimposed turbulence. A hierarchical flight controller and an intra-cycle spooling controller were used to control the kite. Simulations showed robust flight control in the presence of turbulence, along with power production numbers approximately 90 percent as large as in the constant flow case.

REFERENCES

Ampyx (2019). Ampyx Power website.

Fagiano, L., Zgraggen, A.U., Morari, M., and Khammash, M. (2014). Automatic crosswind flight of tethered wings for airborne wind energy: Modeling, control design, and experimental results. *IEEE Transactions on Control Systems Technology*, 22(4), 1433–1447.

Fechner, U. and Schmehl, R. (2016). Flight path control of kite power systems in a turbulent wind environment. In *2016 American Control Conference (ACC)*, 4083–4088. IEEE.

Ghasemi, A., Olinger, D.J., and Tryggvason, G. (2015). Computational simulation of the tethered undersea kites for power generation. In *ASME 2015 International Mechanical Engineering Congress and Exposition*, V06BT07A043–V06BT07A043. American Society of Mechanical Engineers.

Ghasemi, A., Olinger, D.J., and Tryggvason, G. (2016). A nonlinear computational model of tethered underwater kites for power generation. *Journal of Fluids Engineering*, 138(12).

Haas, K.A., Fritz, H.M., French, S.P., and Neary, V. (2013). Assessment of energy production potential from ocean currents along the United States coastline. Georgia Tech Research Corporation.

Haas, K.A., Fritz, H.M., French, S.P., Smith, B.T., and Neary, V. (2011). Assessment of energy production potential from tidal streams in the United States. Georgia Tech Research Corporation.

Jacobson, P. (2011). Mapping and assessment of the united states ocean wave resource. Electric Power Research Institute (EPRI).

Li, H., Olinger, D.J., and Demetriou, M.A. (2015). Control of a tethered undersea kite energy system using a six degree of freedom model. In *2015 54th IEEE Conference on Decision and Control (CDC)*, 688–693. IEEE.

LiVecchi, A., Copping, A., Jenne, D., Gorton, A., Preus, R., Gill, G., Robichaud, R., Green, R., Geerlofs, S., Gore, S., Hume, D., McShane, W., Schmaus, C., and Spence, H. (2019). Powering the blue economy: Exploring opportunities for marine renewable energy in maritime markets. *U.S. Department of Energy*.

Loyd, M. (1980). Crosswind kite power. *Journal of Energy*, 4(3), 106–111.

Makani (2019). Makani website.

Minesto (2019). Minesto, ltd. website.

Mycek, P., Gaurier, B., Germain, G., Pinon, G., and Rivoalen, E. (2014). Experimental study of the turbulence intensity effects on marine current turbines behaviour. Part I: One single turbine. *Renewable Energy*, 66, 729–746.

Olinger, D.J. and Wang, Y. (2015). Hydrokinetic energy harvesting using tethered undersea kites. *Journal of Renewable and Sustainable Energy*, 7(4), 043114.

Pyakurel, P., VanZwieten, J.H., Dhanak, M., and Xiros, N.I. (2017). Numerical modeling of turbulence and its effect on ocean current turbines. *International Journal of Marine Energy*, 17, 84–97.

Rapp, S., Schmehl, R., Oland, E., Smidt, S., Haas, T., and Meyers, J. (2019). A modular control architecture for airborne wind energy systems. In *AIAA Scitech 2019 Forum*, 1419.

Reed, J., Daniels, J., Siddiqui, A., Cobb, M., and Vermillion, C. (2019). Optimal exploration and charging for an autonomous underwater vehicle with energy-harvesting kite. Accepted to American Controls Conference 2020.

Sternberg, J., Goit, J., Gros, S., Meyers, J., and Diehl, M. (2012). Robust and stable periodic flight of power generating kite systems in a turbulent wind flow field. *IFAC Proceedings Volumes*, 45(25), 140–145.

Vermillion, C., Grunnagle, T., Lim, R., and Kolmanovsky, I. (2014). Model-based plant design and hierarchical control of a prototype lighter-than-air wind energy system, with experimental flight test results. *IEEE Transactions on Control Systems Technology*, 22, 531–542.

Windlift (2019). Windlift website.

Yang, Z. and Copping, A. (2017). *Marine Renewable Energy: Resource Characterization and Physical Effects*. Springer.

Zeng, X. and He, R. (2016). Gulf Stream variability and a triggering mechanism of its meander in the South Atlantic Bight. *Journal of Geophysical Research - Oceans*, 121.